

EARLY METAL ENRICHMENT BY PREGALACTIC OUTFLOWS: II. SIMULATIONS OF BLOW-AWAY

MASAO MORI^{1,2}, ANDREA FERRARA^{2,3}, AND PIERO MADAU^{3,4}

submitted to the ApJ

ABSTRACT

Supernova (SN)-driven pregalactic outflows may be an efficient mechanism for distributing the product of stellar nucleosynthesis over large cosmological volumes prior to the reionization epoch. Here we present results from three-dimensional numerical simulations of the dynamics of SN-driven bubbles as they propagate through and escape the grasp of subgalactic halos with masses $M = 10^8 h^{-1} M_\odot$ at redshift $z = 9$. Halos in this mass range are characterized by very short dynamical timescales (and even shorter gas cooling times), and are therefore likely to form stars in a rapid but intense burst before SN ‘feedback’ quenches further star formation. The hydrodynamic simulations use a nested grid method to follow the evolution of explosive multi-SN events operating on the characteristic timescale of a few $\times 10^7$ yr, the lifetime of massive stars. The results confirm that, if the star formation efficiency of subgalactic halos is close to 10%, a significant fraction of the halo gas will be lifted out of the potential well (‘blow-away’), shock the intergalactic medium, and pollute it with metal-enriched material, a scenario recently advocated by Madau, Ferrara, & Rees (2001). The volume filling factor of the ejecta is close to unity. Depending on the stellar distribution, we find that less than 30% of the available SN energy is converted into kinetic energy of the blown away material, the remainder being radiated away. It appears that mechanical feedback is less efficient than expected from simple energetic arguments, as off-nuclear SN explosions drive inward-propagating shocks that tend to collect and pile up cold gas in the central regions of the host halo. Low-mass galaxies at early epochs may survive multiple SN events and continue forming stars.

Subject headings: cosmology: theory – galaxies: formation – hydrodynamics – intergalactic medium – supernovae: general

1. INTRODUCTION

In currently popular hierarchical clustering scenarios for the formation of cosmic structures – all variants of the cold dark matter (CDM) cosmogony – the assembly of galaxies is a bottom-up process in which large systems result from the merging of smaller subunits. In these theories dark matter halos with masses $M = 10^8 h^{-1} M_\odot$ collapse at $z \approx 10$ from 2σ density fluctuations: the gas infalling along with the dark matter perturbation is shock-heated to the virial temperature $T_{\text{vir}} = 2 \times 10^4$ K, condenses rapidly due to atomic line cooling, and becomes self-gravitating. Massive stars then form with some initial mass function (IMF), synthesize heavy-elements, and explode as supernovae (SNe) after a few $\times 10^7$ yr, enriching the surrounding medium. These subgalactic stellar systems, possibly aided by a population of accreting black holes in their nuclei and/or by an earlier generation of stars in even smaller halos (‘minihalos’ with virial temperatures of only a few hundred kelvins, where collisional excitation of molecular hydrogen is the main coolant), are believed to have generated the ultraviolet radiation and mechanical energy that reheated and reionized the universe (see Barkana & Loeb 2000 for a recent review).

It is a simple expectation of the above scenario that the energy deposition by SNe in the shallow potential wells of subgalactic systems may have two main effects, depending

on the efficiency with which halo gas can cool and fragment into clouds and then into massive stars: (i) the disruption of the newly formed object, i.e. the most violent version of the so-called ‘stellar feedback’ (Larson 1974; Dekel & Silk 1986; Mori et al. 1997; Mori, Yoshii, & Nomoto 1999; MacLow & Ferrara 1999; D’Ercole & Brighenti 1999; Murakami & Babul 1999; Ferrara & Tolstoy 2000; Ciardi et al. 2000); and (ii) the blow-away of metal-enriched baryons from the host (dwarf) galaxy, causing the pollution of the IGM at early times (Tegmark, Silk, & Evrard 1993; Voit 1996; Nath & Trentham 1997; Gnedin & Ostriker 1997; Ferrara, Pettini, & Shchekinov 2000; Madau, Ferrara, & Rees 2001, hereafter Paper I). The well-established existence of heavy elements like carbon, nitrogen, and silicon in the Ly α forest clouds at $z = 3-3.5$ may be the best evidence for such an early episode of pregalactic star formation and outflows (Songaila 1997; Ellison et al. 2000). Stellar feedback and galactic outflows at high-redshifts may also temporarily halt or delay the formation of dwarf galaxies (Scannapieco & Broadhurst 2001; Scannapieco, Ferrara, & Broadhurst 2000), affect the thermal state of the IGM (Madau 2000; Theuns, Mo, & Schaye 2001; Cen & Bryan 2001), and play a crucial role during the reionization epoch (Ciardi et al. 2000; Bruscoli et al. 2000).

This is the second paper in a series aimed at a detailed

¹Institute of Natural Science, Senshu University, Kawasaki-shi, Kanagawa-ken, 214-8580, Japan.

²Center for Computational Physics, University of Tsukuba, Tsukuba-shi, Ibaraki-ken, 305-8577, Japan.

³Osservatorio Astrofisico di Arcetri, Largo Enrico Fermi 5, 50125 Firenze, Italy.

⁴Department of Astronomy and Astrophysics, University of California, Santa Cruz, CA 95064.

study of stellar feedback and SN–driven pregalactic outflows at early epochs. In Paper I it was shown that the observed narrow Doppler widths and inferred large filling factor of chemically enriched, low–density Ly α forest clouds may point to a more uniform (i.e. ‘early’) rather than in–situ (i.e. ‘late’) cosmic metal pollution. Whilst outflows of metal–rich gas are directly observed in Lyman–break galaxies at $z \approx 3$ (Pettini et al. 2000), most of this gas may not leave the immediate surroundings of these deep gravitational potential wells. We argued that, if intergalactic metals were actually dispersed *over large cosmological volumes* from massive galaxy halos at late times, such a delayed epoch of galactic “super–winds” would have severely perturbed the IGM (since the kinetic energy of the ejecta is absorbed by intergalactic gas), raising it to a much higher adiabat than expected from photoionization, and producing large spatial variations of the baryons relative to the dark matter. This would make the success of cosmological hydrodynamical simulations in matching the overall observed properties of Ly α absorption systems largely coincidental. Alternatively, the observations could be more easily explained if the ejection of heavy elements at velocities exceeding the small escape speed of numerous subgalactic systems were to take place at very high redshifts. This is because hot enriched material cools more efficiently at these early epochs, and the expansion of SN–driven bubbles into a dense IGM (pre–photoionized by the same massive stars that later explode as SNe) would be halted by the external pressure. In this scenario, any residual peculiar velocity would have been redshifted away by $z = 3$, the Ly α forest would be hydrodynamically ‘cold’, and the intergalactic baryons would have relaxed again under the influence of dark matter gravity.

In Paper I the most efficient pollutant of the IGM on large scales were identified as subgalactic systems with masses $\sim 10^8 h^{-1} M_\odot$ at $z \sim 10$, when large number of them grow non–linear and collapse. We showed how stellar feedback in these pregalactic halos (with virial temperatures $T_{\text{vir}} = 2 \times 10^4 \text{ K}$, i.e. at the peak of the cooling curve for primordial gas) may be an inherently different process than that often invoked to prevent the ‘overcooling’ of baryons in the central regions of larger systems (White & Frenk 1991; Cole et al. 1994; Navarro & Steinmetz 1997, 2000). This is because such fragments are characterized by very short dynamical timescales (and even shorter gas cooling times): throughout the halo the accreted baryons condense immediately due to atomic hydrogen cooling, and the supply of cold gas for star formation is only limited by the infall rate. They are therefore expected to go through a rapid but intense star forming phase, since one cannot assume *instantaneous feedback* from SNe in systems with such a short dynamical timescale. Lacking the ability to store efficiently the corresponding energy input in turbulent and magnetic forms or by relaxing to a multiphase medium, these systems have very limited resources to sustain a self–regulated star formation cycle (cf. Efstathiou 2000).

In Paper I we used the thin shell approximation to model the evolution of SN–driven bubbles as they propagate through and blow out from subgalactic halos. We assumed spatial coherency among SN events and tem-

poral coherency among their progenitors, i.e. all explosions were assumed to take place at the center of the halo, and the progenitor stellar population to form co–equally, on a timescale short compared to the lifetime of massive stars. In this paper we present results from three–dimensional hydrodynamic simulations of the dynamics of SN–driven bubbles in subgalactic halos using a hierarchical nested grid technique. Besides accounting for the mass–dependent main sequence evolutionary timescale of massive stars (as in Paper I), which causes a temporal spread of SN explosions, we also explore the role of different spatial distributions of the explosion sites inside the galaxy, thus relaxing the assumption that all SNe occur at the center. The crucial questions we try to give a quantitative answer in this paper are: How efficient mechanical feedback really is? Can small halos survive multiple SN events and continue forming stars or are they blown away and end their life as ‘naked stellar clusters’ (Ciardi et al. 2000)? How far from the production sites can metals be ejected into the IGM?

2. MODEL ASSUMPTIONS

We will model the structural properties of subgalactic systems following Paper I. We shall assume that virialized dark matter halos, formed through hierarchical clustering, have a universal (spherically averaged) Navarro–Frenk–White (1997, hereafter NFW) density profile,

$$\rho_{\text{DM}}(r) = \frac{\rho_{\text{crit}} \delta_c}{cx(1+cx)^2}, \quad (1)$$

where $x \equiv r/r_{\text{vir}}$, r_{vir} is the virial radius of the system, i.e. the radius of the sphere encompassing a mean overdensity of 200, c is the halo concentration parameter, $\delta_c = (200/3)c^3/F(c)$ is a characteristic overdensity, $\rho_{\text{crit}} = 3H^2/(8\pi G)$ the critical density of the universe⁵ at redshift z , and

$$F(t) \equiv \ln(1+t) - \frac{t}{1+t}. \quad (2)$$

The total within the virial radius is $M = (4\pi/3)200\rho_{\text{crit}}r_{\text{vir}}^3$, and the ‘typical’ concentration parameter of halos at $z = 10$ with $M = 10^8 h^{-1} M_\odot$ is $c = 5$ (Paper I). Note that high–resolution N–body simulations by Bullock et al. (2001) indicates that high–redshift halos are actually less concentrated than expected from the NFW prediction. In this case we may be overestimating the escape speed from subgalactic systems.

For our prototypical pollutor (below the mass scale given above the main coolant is molecular hydrogen and halos are strongly affected by radiative feedback, while above this mass scale cooling is less rapid, halos are more rare, and metals are more efficiently retained by the deeper potential well, see detailed discussion in Paper I), the characteristic virial radius, virial temperature, circular velocity at the virial radius, and escape velocity at the center are

$$r_{\text{vir}} = 0.75 \text{ kpc} M_8^{1/3} h^{-1} \left(\frac{1+z}{10} \right)^{-1}, \quad (3)$$

⁵Throughout this paper we assume an Einstein–de Sitter universe and a Hubble constant of $H_0 = 100 h \text{ km s}^{-1} \text{ Mpc}^{-1}$. The numerical simulations are run with $h = 0.5$.

$$T_{\text{vir}} = 2 \times 10^4 \text{ K} M_8^{2/3} \left(\frac{1+z}{10} \right), \quad (4)$$

$$V_c = 24 \text{ km s}^{-1} M_8^{1/3} \left(\frac{1+z}{10} \right)^{1/2}, \quad (5)$$

$$v_e(0) = 77 \text{ km s}^{-1} M_8^{1/3} \left(\frac{1+z}{10} \right)^{1/2}, \quad (6)$$

respectively, where M_8 is the halo mass in units of $10^8 h^{-1} \text{ M}_\odot$. Here we have set the mean molecular weight μ to 0.59, appropriate for a fully ionized primordial gas. At the virial radius $v_e(r_{\text{vir}}) = 0.62 v_e(0)$. If baryons virialize in the dark matter halo to an isothermal distribution, they will be shock-heated to the virial temperature and settle down to a density profile

$$\begin{aligned} \ln \rho(r) &= \ln \rho_0 - \frac{\mu m_p}{2kT_{\text{vir}}} [v_e^2(0) - v_e^2(r)] \\ &= \ln \rho_0 - \frac{2c}{F(c)} \left[1 - \frac{\ln(1+cx)}{cx} \right], \end{aligned} \quad (7)$$

where m_p is the proton mass. The central gas density ρ_0 is determined by the condition that the total baryonic mass fraction within the virial radius is equal to Ω_b initially. Adopting $\Omega_b h^2 = 0.019$ (Burles & Tytler 1998), one gets $\rho_0 = 840 h^{-2} \rho_{\text{crit}} = 1.6 \times 10^{-23} \text{ gr cm}^{-3}$ at $z = 9$. The halo gas density at r_{vir} is $\rho(r_{\text{vir}}) = 0.00144 \rho_0 = 2.3 \times 10^{-26} \text{ gr cm}^{-3}$. This is about 60 times lower at $(1+z) = 10$ than the IGM density, to avoid unphysical effects due to this jump we have allowed the two distributions to merge through a hyperbolic tangential transition of width $0.05 r_{\text{vir}}$.

2.1. Supernova progenitors

As shown in Paper I, for halo masses in the range $10^8 h^{-1} \lesssim M \lesssim 10^{10} h^{-1} \text{ M}_\odot$ at $(1+z) = 10$, the cooling time is shorter than the dynamical timescale everywhere in the halo: infalling gas never comes to hydrostatic equilibrium, but collapses to the center at the free-fall rate. In our prototypical halo, the free-fall time is 10^7 yr at $r = 0.1 r_{\text{vir}}$, increasing to $8 \times 10^7 \text{ yr}$ at r_{vir} (Paper I). The cooling time for gas at T_{vir} is always shorter than the free-fall time by more than two orders of magnitude. Mechanical energy will be injected by SNe only after a few times 10^7 yr : at this stage SN-driven bubbles will propagate into the halo quenching further star formation, and the conversion of cold gas into stars will be limited by the increasing fractional volume occupied by supernova remnants. Before this SN feedback starts operating, as much as 20–30% of the halo gas may be able to cool, fragment, and form stars. Small pregalactic systems at early times, like the ones under consideration, may then be expected to consume a fair fraction of their cold gas in a single burst of star formation. Note that the highest efficiency estimated in nearby star-forming regions is about 30% for the Ophiuchi dark cloud (Wilking & Lada 1983; Lada & Wilking 1984), and that the UV radiation from massive stars may further inhibit cooling and delaying the collapse of mildly overdense regions (Nishi & Tashiro 2000). In the following we will adopt an illustrative value of $f_\star = 10\%$ for the star formation efficiency.

The halo under study has a baryonic mass $M_b = \Omega_b M = 0.019 h^{-2} \times 10^8 h^{-1} \text{ M}_\odot = 1.9 \times 10^6 h^{-3} \text{ M}_\odot$. Its total stellar mass is then $M_\star = f_\star M_b = 1.5 \times 10^6 \text{ M}_\odot$ ($h = 0.5$).

An amount M_\star of baryons is subtracted from the total gas mass; the rest of the gas is assumed to keep the same initial distribution. We assume that the initial stellar mass function (IMF) can be approximated by a Salpeter power-law with lower and upper mass cutoffs equal to $m_l = 0.1 \text{ M}_\odot$ and $m_u = 120 \text{ M}_\odot$, respectively. Note that considerable uncertainties still remain on the characteristic mass of the first luminous objects. Numerical simulations of the fragmentation of primordial clouds with masses \gtrsim a few $\times 10^5 \text{ M}_\odot$ in hierarchical cosmogonies have suggested that the IMF of the very first, zero-metallicity stars forming at $z \gtrsim 20$ may be extremely top-heavy (Bromm, Coppi, & Larson 1999, 2001a; Abel, Bryan, & Norman 2000), perhaps giving origins to a population of pregalactic massive black holes (Madau & Rees 2001). As this feature appears linked to primordial H₂ chemistry and cooling, at the later epochs of interest here and in more massive halos where gas condense due to atomic line cooling, it is plausible that a ‘second’ generation of stars may be able to form with an IMF that is less biased towards very high stellar masses. This scenario is further supported by the recent findings of Bromm et al. 2001b.

In our simulation, the mass of each star is determined by randomly sampling the IMF until the total stellar mass is equal to M_\star ; SN progenitors are then identified as those stars more massive than 8 M_\odot . We find that a total number of $N_t = 11170$ SNe are produced in the system, out of 4.24×10^6 stars (average stellar mass = 0.35 M_\odot) yielding a SN every 134 M_\odot of stars formed. Each massive stars (with mass m in units of M_\odot) explodes after a main sequence lifetime of

$$\log t_{\text{ms}} \text{ (yr)} = 10.025 - 3.559 \log m + 0.898(\log m)^2. \quad (8)$$

This is a fit to a compilation of the available data in the literature (Schaller et al. 1992; Vacca, Garmany & Shull 1996; Schaerer & de Koter 1997; Palla, private communication). In the local universe SNe are known not to occur at random location but rather to cluster into OB associations (Heiles 1990). In nearby galaxies the luminosity function of OB associations is well approximated by a power-law

$$\frac{d\mathcal{N}_{\text{OB}}}{dN} = AN^{-\beta}, \quad (9)$$

with $\beta \approx 2$ (McKee & Williams 1997; Oey & Clarke 1998). Here \mathcal{N}_{OB} is the number of associations containing N OB stars; the probability for a cluster of OB stars to host N SNe is then $\propto N^{-2}$. We apply a grouping procedure according to the above distribution: this yields 90 OB associations, each containing a variable number of massive stars ranging from a few tens to up to 2000. For numerical reasons to be discussed below, we set a lower limit to the number of stars in an association equal to 20. As a final step we have to spatially locate the 90 associations in the halo. We distribute them according to a Schmidt-type law, i.e. their density is $\propto \rho^\alpha$, with $\alpha = 1, 2$. The two cases correspond to a relatively extended ($\alpha = 1$) or more centrally concentrated ($\alpha = 2$) star formation volume (in the limit $\alpha \rightarrow \infty$ all SNe explode at the center). We will refer to them in the following as Case 1 ($\alpha = 1$) and Case 2 ($\alpha = 2$), respectively.

3. PRELIMINARY CONSIDERATIONS

Before discussing the detailed results of the numerical simulations, it is important to provide some physical insights into the problem.

3.1. Effects of explosion location

In order for the gas to be ejected from the galaxy, a necessary condition implies that the initial energy provided by the supernovae has to be larger than the gravitational one. The latter is given by

$$E_g = \frac{1}{2} \int_V d^3 \mathbf{r} \rho(r) \phi(r) \quad (10)$$

where $\phi(r) = -GM(r)/r$ is the gravitational potential. With the gas density distribution given by equation (7), integration yields

$$\begin{aligned} E_g &= \frac{3 V_c^2 M}{400 F(c)} \int_0^1 dx x F(cx) \left(\frac{\rho}{\rho_{\text{crit}}} \right) = 0.01 h^{-2} V_c^2 M \\ &= 10^{52} h^{-3} \text{ erg} \left(\frac{1+z}{10} \right) M_8^{5/3}. \end{aligned} \quad (11)$$

This energy must be compared with the total mechanical energy injected by SN explosions, $E_{\text{SN}} = N_t E_0 = 1.1 \times 10^{55} \text{ erg}$. The naive conclusion would be that this energy deposition, being roughly hundred times higher than the gas binding energy, should produce a complete blow-away of the halo. There are two main reasons, however, for why this is not actually the case: i) the conversion efficiency of E_{SN} into kinetic energy of the interstellar medium (ISM) is well below unity since radiative energy losses, particularly at the halo center where the baryon density is initially $n(0) \approx 10 \text{ cm}^{-3}$, carry away a significant fraction of this energy; and ii) as the explosion sites are scattered within the host galaxy, they can have very different effects. For example, explosions taking place in the outer halo will tend to expand outwards along the rapidly decreasing density gradient: the released energy will be eventually used to energize the IGM. Off-nuclear SN explosions will drive inward-propagating shocks that pile up and compress the gas in the central regions, further increasing radiative losses. Also, energy deposition by an association at the center may never accelerate material beyond the virial radius.

We can better quantify the last point by adopting the following zeroth order approximation. We treat each association as a point explosion (in practice, due to the spread of the various SN events, the ensuing superbubble is better described by a wind solution, see Paper I). The evolution of a point explosion in a stratified medium can be treated by the thin-shell approximation. This solution accurately approximates the exact numerical results (see, e.g., MacLow et al. 1989) and can be obtained from dimensional analysis. The shell velocity is $v_s(r) \simeq [P/\rho(r)]^{1/2}$, where the pressure P is roughly equal to E/X^3 : $E = NE_0$ is the energy injected by N SNe in the association. The explosion is allowed to take place at different radial positions $x_0 = r_0/r_{\text{vir}}$; the bubble size along the radial coordinate is then $X = r_{\text{vir}}(x - x_0)$. We can then calculate the value of $v_s(r_{\text{vir}})$, which can then be compared to the escape velocity $v_e(r_{\text{vir}})$ to get an idea of the final fate (escape versus

recapture) of the ejected gas. The results are shown in Figures 1 and 2 as $v_s(r_{\text{vir}})$ isocontours in the plane identified by x_0 and N . Also shown are the locations in that plane of the associations used in the numerical simulations for the two cases considered. It can be seen that, if the explosion occurs at the halo center ($x_0 = 0$), a minimum of about 50 SNe is required in order to achieve shell velocities in excess of $v_e(r_{\text{vir}})$. This constraint is much weaker at (say) $x_0 = 0.7$, where even a single SN event can produce the same effect. Thus, every explosion occurring beyond this location will easily lead to mass loss from the galaxy. Note that in Case 1 a larger fraction (about 90%) of SN events will give origin to significant mass loss, as they take place preferentially in the galactic outskirts. By contrast, in Case 2 about 1/3 of the OB associations generate only sub-escape speeds, i.e. $v_s(r_{\text{vir}}) < v_e(r_{\text{vir}})$.

3.2. Energy- and mass-carrying winds

Explosions located in the halo outer regions produce higher velocities of the outflowing material. The swept-up mass, however, decreases as the halo density is lower in the outskirts. In this case SNe basically vent energy (an energy-carrying wind) into the IGM, but little galactic mass. An accurate determination of the kinetic energy carried away, $E_k \propto M_s v_s^2$, can only be done numerically as it depends on the detailed mass loading of the propagating shells. To get some insight, we estimate the kinetic energy flux through r_{vir} as

$$\mathcal{E}_k(x_0, N) = v_s^2(r_{\text{vir}}) \Sigma(x_0) = \frac{NE_0 r_{\text{vir}}}{X^3 \rho} \int_{x_0}^1 dx \rho, \quad (12)$$

where $\Sigma(x_0)$ is the halo gas (mass) column density along the radial direction from x_0 to r_{vir} . We then plot in Figure 3 the column Σ normalized to the total column through the halo center, Σ_t , as a function of the square of the ratio $v_s(r_{\text{vir}})/v_e(r_{\text{vir}})$. If the kinetic energy flux were the same at every location one would find $\Sigma v_s^2(r_{\text{vir}}) = \text{const} = \mathcal{E}_k(N)$. As seen from Figure 3, however, the trend is rather different. For $N = 10$ the curve drops very rapidly below the one for $\mathcal{E}_k(10)$: this is because the increase in the shell velocity cannot compensate for the drop in mass as the explosion is displaced from the origin. It is only in the outskirts ($x_0 > 0.75$) that the transition to a predominantly energy-carrying wind occurs. In the $N = 100$ case such inversion is not seen, essentially because the mass decrease always dominate over the velocity increase.

In conclusion, if SNe occur in small $N \approx 20 - 30$ associations (or are isolated), either there is no mass-loss (if they are located at the center) or they mostly inject energy rather than mass into the IGM (if they are located in the outer halo). It is only when they are grouped together in larger associations that they will be able to eject both mass and energy into the intergalactic space.

3.3. Porosity and amplification effect

Based on the results shown in Figures 1 and 2, Case 2 should lead to a smaller mass loss from our subgalactic halo. This, however, may not be necessarily the case, as “amplification” effects can be important in the central regions. Due the high stellar density at $x < 0.2$ (say),

overlapping of the hot bubble interiors does occur if cooling is not too strong. In this case, the energy deposited at the various explosion sites can add and act coherently on the same shell, leading to an amplification of the pressure force and to higher shell velocities. In other words, the porosity of the hot gas, Q , (its volume filling factor being equal to $1 - e^{-Q}$) is a key parameter, as already pointed out by Silk (1997) and Efstahtiou (2000) in the context of feedback-regulated star formation in galaxy disks. The effect of the interaction and merging of individual bubbles will be discussed in the framework of the numerical simulations discussed below.

4. NUMERICAL METHOD

The evolution of the gas is described by the three-dimensional hydrodynamic equations for a perfect fluid in Cartesian geometry. The continuity equation (including a term due to mass ejection from SNe, ρ_s), the momentum equation with the gravitational acceleration $\mathbf{g} = (g_x, g_y, g_z)^T$, and the thermal energy equation associated with the rates of cooling Λ and SNe heating Γ_s , can be written in compact form as

$$\frac{\partial \mathbf{U}}{\partial t} + \frac{\partial \mathbf{F}}{\partial x} + \frac{\partial \mathbf{G}}{\partial y} + \frac{\partial \mathbf{H}}{\partial z} = \mathbf{S} \quad (13)$$

with

$$\mathbf{U} = (\rho, \rho v_x, \rho v_y, \rho v_z, \rho e)^T, \quad (14)$$

$$\mathbf{F} = (\rho v_x, \rho v_x^2 + p, \rho v_x v_y, \rho v_x v_z, \rho v_x h_e)^T, \quad (15)$$

$$\mathbf{G} = (\rho v_y, \rho v_x v_y, \rho v_y^2 + p, \rho v_y v_z, \rho v_y h_e)^T, \quad (16)$$

$$\mathbf{H} = (\rho v_z, \rho v_x v_z, \rho v_y v_z, \rho v_z^2 + p, \rho v_z h_e)^T, \quad (17)$$

$$\mathbf{S} = (\dot{\rho}_s, \rho g_x, \rho g_y, \rho g_z, \rho \mathbf{v} \cdot \mathbf{g} + \Gamma_s - \Lambda)^T. \quad (18)$$

Here \mathbf{U} is a state vector of conserved quantities, \mathbf{F} , \mathbf{G} , and \mathbf{H} are the corresponding flux vectors, and \mathbf{S} is the source-term vector that includes sources and sinks of conserved quantities, such as heating and cooling terms and the gravitational acceleration. Also, ρ is the gas density, $\mathbf{v} = (v_x, v_y, v_z)^T$ is the gas velocity vector,

$$e = \varepsilon + \frac{1}{2}|\mathbf{v}|^2 = h_e - \frac{p}{\rho} \quad (19)$$

is the specific total energy, h_e is the enthalpy, and the internal energy ε is related to the gas pressure by

$$p = (\gamma - 1)\rho \varepsilon, \quad (20)$$

where γ ($=5/3$) is the adiabatic index.

The equations are solved by a finite volume scheme with operator splitting, which is based on the AUSMDV described by Wada & Liou (1997). Liou & Steffen (1993) developed a remarkably simple upwind flux vector splitting scheme called ‘advection upstream splitting method’ (AUSM). It treats the convective and pressure terms of the flux function separately. The AUSMDV has a blending form of AUSM and flux difference, and improves the robustness of AUSM in dealing with the collision of strong shocks. We extended it to third-order spatial accuracy using MUSCL (van Leer 1977) with a total variation diminishing limiter proposed by Arora & Roe (1997). Since

this scheme has a great advantage due to the reduction of numerical viscosity, fluid interfaces are sharply preserved and small-scale features can be resolved as in the ‘piecewise parabolic method’ (PPM) of Woodward & Colella (1984). The AUSMDV scheme is, however, simpler and has a lower computational costs than PPM.

One of the main purposes of our study is to determine how far from the production sites can the product of stellar nucleosynthesis propagate into the IGM. Thus, we have to deal with very different length scales in our simulation. If we assume, e.g., a minimum resolution length comparable to the scale of an individual SN remnant, ~ 30 pc, and set the size of the simulation box to forty times the virial radius of the halo, i.e. 60 kpc for $h = 0.5$, then about 2,000 zones are needed per dimension. Even with massive supercomputers, it is difficult to carry out such a simulation in three-dimensions. We have therefore adopted a 3-D ‘nested grid method’. Our scheme is similar to Tomisaka’s (1996) two-dimensional version: the general algorithm is based on the works of Berger & Oliger (1984) and Berger & Colella (1989). Six levels of fixed Cartesian grids were used, with every fine grid being completely covered by a coarser one. We named the grids L1 (the finest), L2, ..., L6 (the coarsest), as shown in the right panel of Figure 4. The box size of grid L1 was set equal to $2r_{\text{vir}}$, and the mesh size of the L_n grid to twice that of the $L_n - 1$ level. All grids were centered within each other, with the finest covering the whole galaxy halo. Since the cell number is the same ($128 \times 128 \times 128$) for every level L_n ($n = 1, 2, \dots, 6$), the minimum resolved scale is about 22 pc and the size of the coarsest grid is 96 kpc. Thus, the scheme has a wide dynamic range in the space dimension.

The grids are connected by the transfer of conserved variables: the mass density ρ , the components of the momentum density $\rho \mathbf{v}$, and the total energy density ρe . Since each coarse cell is resolved by exactly 2^3 fine cells, the part of the coarse grid covered by the finer grid is overwritten with the arithmetic averages of these variables on 8 fine cells. The boundary conditions for a fine grid are determined instead by monotonic interpolation of physical variables on the coarser grid. For the coarsest level L6 we adopt outflowing boundary conditions by imposing for each variable a zero gradient. Since the Courant–Friedrichs–Lowy condition requires the time-step of a coarser grid to be twice as long as the time-step of the next finer level, the finer grids must be calculated much more often. The finest grid (L1) is calculated first using an appropriate time-step Δt . After two time-steps of finest grid, the grid one level coarser is advanced by the time-step of $2\Delta t$. The scheme is repeated recursively until all grids are advanced. Every time the sequence changes from a fine to a coarse grid, the data on the fine grid are averaged onto the coarse one.

The center of the fixed NFW dark matter potential is located at the center of the simulation boxes, and the halo initial gas distribution follows equation (7). The halo gas is assumed to be non self-gravitating, of primordial composition, optically thin, and in collisional ionization equilibrium. We assume that the metal ejecta either do not mix with the ambient gas or do so at late times (cf. Paper I). Even if some mixing occurs inside the hot cavity gas thereby increasing its metallicity, because of the very low density of this gas the cooling rate should remain much

lower than in the outer cooling shell. The external IGM is at $T = 10,000$ K, as expected from photoheating by the SN progenitors. We use the radiative cooling function of Sutherland & Dopita (1993) for primordial gas, and include the effect of Compton cooling off microwave background photons,

$$\Lambda_c = (5.4 \times 10^{-36} \text{ erg cm}^{-3} \text{ s}^{-1}) \chi \rho (1+z)^4 T. \quad (21)$$

Here χ is the ionized fraction, z ($=9$) is the redshift, and T is the gas temperature. The cooling and heating terms are integrated implicitly.

Mechanical feedback from SNe is a critical process in galaxy formation studies and simulations, as it modifies the composition and thermodynamical state of the ambient gas. Different approximate prescriptions have been adopted in the past, largely imposed by numerical limitations and a poor appreciation of how to implement feedback in hydrodynamical simulations (Katz 1992; Navarro & White 1993; Mihos & Hernquist 1994; Mori et al. 1997; MacLow & Ferrara 1999; Mori, Yoshii, & Nomoto 1999). Navarro & White (1993) and Mihos & Hernquist (1994) assumed that a fraction f_v of the available SN explosion energy is deposited in the ambient gas as a radial velocity perturbation directed away from the event, the remainder being dumped as heat. This method is obviously rather sensitive to the assumed value for f_v . Mori et al. (1997) and Mori, Yoshii, & Nomoto (1999) assumed that the gas within the maximum radius of the shock front in the adiabatic phase of a supernova remnant (Shull & Silk 1979) remains adiabatic until the multiple SNe II phase ends at $t_{\text{ms}}(8 \text{ M}_\odot)$. In this case, the effects of radiative cooling might have been underestimated. MacLow & Ferrara (1999) modeled SN feedback in a central region of a dwarf galaxy as a constant luminosity wind driven by a thermal energy source. Nearby starbursts, however, are known to have multiple star formation sites scattered across the whole galaxy.

Our algorithm for simulating SN feedback improves upon previous treatments in several ways. OB associations are distributed as a function of gas density ($\propto \rho^\alpha$) using a Monte-Carlo procedure (the projected distributions of associations in plotted in Figure 4). After a main sequence lifetime, all stars more massive than 8 M_\odot explode instantaneously injecting an energy of 10^{51} erg, and their outer layers are blown out leaving a compact remnant of 1.4 M_\odot . Therefore SNe inject energy (assumed in pure thermal form) and mass into the interstellar medium: these are supplied to a sphere of radius

$$R_s = 24 \text{ pc} \left(\frac{\Delta t}{10^4 \text{ yr}} \right)^{2/5} \left(\frac{n}{0.1 \text{ cm}^{-3}} \right)^{-1/5}, \quad (22)$$

corresponding to the radius of a SN remnant in a uniform ambient medium of density n and in the adiabatic Sedov-Taylor phase; the expansion velocity \dot{R}_s is also self-consistently calculated from such solution. The gas then starts cooling immediately according to the adopted gas cooling function. The radius R_s has a minimum value of 22 pc due to numerical resolution. The time-step Δt is controlled by the Courant condition. One additional constraint is that, if there are more than two SN events in a OB association, we decrease Δt until only one explosion per association occurs during the time-step Δt . The

main limitation of our method is the assumption that the gas is initially in hydrostatic equilibrium and non self-gravitating.

5. NUMERICAL RESULTS

As mentioned above, we have run two numerical simulations, an extended stellar distribution (Case 1) and a more concentrated one (Case 2). In both runs 11170 SNe explode in our halo (corresponding to $f_\star = 10\%$). Snapshots of the gas density and temperature distributions in a slice along the X-Y plane of the nested grids are shown in Figures 5 and 6 for Case 1, and Figures 7 and 8 for Case 2. The three columns in each figure depict the time evolution from about 5 Myr to up to 200 Myr. Along a given row, the leftmost panel refers to grid L5 (linear size 48 kpc), the central one to grid L3 (linear size 12 kpc), and the rightmost panel refers to the grid L1 (linear size 3 kpc). The density range is $-5 \leq \log (n/\text{cm}^{-3}) \leq 1$, and the temperature range is $4 \leq \log (T/\text{K}) \leq 8.5$.

After a few Myr from the beginning of the simulation the most massive stars explode as SNe and produce expanding hot bubbles surrounded by a cooling dense ($n \approx 1 \text{ cm}^{-3}$) shell. At these early times the typical bubble size tends to be larger in Case 1 than in Case 2 because in the former scenario the explosions sites are more uniformly distributed and more likely to occur in the outer, lower-density regions, which favors their rapid expansion. In spite of the smaller typical bubble size, the degree of overlapping appears to be more pronounced in Case 2, indicating that the crowding effect is dominant.

The different initial topology of the multiphase ISM leaves an imprint also in the later evolutionary stages. At around 10 Myr the ISM structure is relatively ordered in Case 2, where individual bubbles have merged in a coherent (although far from spherical) expanding superbubble from which cold ($T \approx 10^4$ K) filaments protrude inside the cavity. These filaments are the leftovers of previous individual shell-shell interactions further processed by hydrodynamic instabilities. In Case 1, the halo topology is more perturbed, with bubbles expanding in the outer regions having already undergone blowout and venting their hot gas into the IGM (see, e.g., the structure at the top of the panel in the second row, third column of Fig. 5), and others whose interaction is giving rise to an intricated, multiphase structure in the inner halo, where 10^8 K gas co-exists with a cooler 10^4 K phase from which it is separated by cooling interfaces. Note that for Case 1 SN explosions in the outer halo drive inward-propagating shocks that act to collect and pile up gas towards the center. This effect is much less pronounced in Case 2 where the net mass flow is an expanding one. As we will see below, the impact of the mechanical energy deposition on the host pregalactic halo is rather different in the two simulations.

As the evolution continues, a coherent and increasingly spherical shell expanding into the IGM is eventually formed in both runs. The shell contains a large fraction of the halo gas that has been swept-up during the evolution; at $t = 20$ Myr its size is roughly 6 kpc for Case 1 and slightly larger for Case 2, as a consequence of the most efficient use of mechanical energy in the latter simulation. In Case 1 one can clearly see a central, dense core resulting from the ‘implosion’ wave mentioned above. While such a

feature is almost absent in Case 2 at $t = 35$ Myr, a dense core will form at later stages as a result of the accretion of cold clumps that are ballistically raining towards the center.

The final two bottom rows of the simulation figures show the final stages of the evolution that are qualitatively similar to the one just described. The shell is now nearly spherically symmetric: its interior is filled with warm ($T \lesssim 10^6$ K) gas at a very low density $n \lesssim 10^{-4}$ cm $^{-3}$, i.e. slightly below the mean value for the IGM. Figure 9 shows the locus of the spherically-averaged shell radius r_{shell} as a function of time. The shell initially follows an energy-driven phase where $r_{\text{shell}} \propto t^{3/5}$ (Weaver et al. 1977). At later time the evolution relaxes to the adiabatic Sedov–Taylor solution with $r_{\text{shell}} \propto t^{2/5}$. Afterwards the shell slows down to a momentum-conserving ‘snow-plough’ phase, $r_{\text{shell}} \propto t^{1/4}$. Figure 9 shows that, at the end of the simulations, the shell is still sweeping out IGM material; its radius and velocity are 21 kpc and 26 km sec $^{-1}$ at $t = 250$ Myr. At Mach number $\mathcal{M} = 1$, as the shock will decay into sound waves, the maximum ‘stalling radius’ will be reached. Using momentum conservation we estimate the final radius of the shell to be close to 26 kpc. This is about a factor 2.3 larger than the value we derived analytically in Paper I for the same case.

In both simulations runs the final configuration includes a central core resulting from the two different mechanisms already outlined; its central density and radial profile is similar to the initial one. However, the relative ratio between the gas mass contained in the shell and the one in the central core is different. A visual inspection of Figures 5 and 7 already shows a thicker shell and a less massive core in Case 2 relative to Case 1. This is confirmed quantitatively by the plots in Figure 10 (Case 1) and Figure 12 (Case 2) where we show the fraction of the initial halo baryonic mass contained inside $(1, 0.5, 0.1)r_{\text{vir}}$ as function of time. The differences are striking: in Case 1, the amount of gas at the center is constantly increasing, finally collecting inside 0.1 r_{vir} about 30% of the total initial mass. On the contrary, in Case 2 the central regions remain practically devoided of gas until 60 Myr, when the accretion process starts. The final result is a small core containing a mass fraction of only 5%. In the former case 50% of the halo gas mass is ejected together with the shell, whereas in Case 2 this fraction is $\sim 85\%$, i.e. the blow-away is nearly complete.

The gas thermal history is illustrated in Figures 11 (Case 1) and 13 (Case 2), where the evolution of the filling factor of the components with temperature larger than a given threshold [$\log(T/\text{K}) = 4, 5, 6, 7, 8$] is shown inside r_{vir} . In both simulations we observe an initial conversion of cold gas into hot gas followed by the opposite, much slower, process. The main difference between the two runs consists in the larger extension of the warm $T = 10^{5-6}$ K component filling 20–50% of the volume in Case 2 at 120 Myr. Also the compression suffered in the inner regions results for Case 1 in a very compact cold gas core, confined to 25% of the volume by 60 Myr, which re-expands afterwards. Case 2 produces a more extended hot gas distribution as seen from the final values of the curves at 120 Myr.

Figure 14 shows the kinetic energy flux, \mathcal{E}_k , carried by

the outflowing gas through the virial radius. The kinetic energy flux is calculated as

$$\mathcal{E}_k = 4\pi r_{\text{vir}}^2 \bar{F}, \quad (23)$$

with

$$\bar{F} = \sum_i dV_i \frac{1}{2} \rho_i v_{ri}^3 / \sum_i dV_i, \quad (24)$$

where dV_i is a volume of the grid cell located at r_{vir} from the center, and ρ_i and v_{ri} are the gas density and the radial velocity at that location, respectively. The summation is taken only for the case of a positive radial velocity at the virial radius. The mean SN mechanical luminosity, L_{SN} , is defined as

$$L_{\text{SN}} = \frac{E_{\text{SN}}}{t_{\text{ms}}(8M_{\odot}) - t_{\text{ms}}(120M_{\odot})}, \quad (25)$$

$$= 1.1 \times 10^{40} \text{ erg s}^{-1}. \quad (26)$$

From Figure 14, we see that kinetic energy is ejected from the galaxy at roughly a constant fraction 25% of the SN mechanical luminosity from 13 Myr to 35 Myr for the Case 1 run; this value increases to about 40% (but with a larger time spread) from 13 Myr to 35 Myr for the Case 2 run. Averaged over the entire evolution, we find that 23% (30%) of the total SNe energy is converted to the kinetic energy of the outflowing gas for the run of Case 1 (Case 2).

6. SUMMARY AND DISCUSSION

In this Paper we have used three-dimensional hydrodynamic simulations to investigate the dynamics of SN-driven bubbles as they propagate through and escape the grasp of subgalactic halos with masses $M = 10^8 h^{-1} M_{\odot}$ at redshift $z = 9$. Depending on the stellar distribution, we found that less than 30% of the available SN energy is converted into kinetic energy of the blown away material, and that mechanical feedback is less efficient than expected from simple energetic arguments, as off-nuclear SN explosions drive inward-propagating shocks that tend to collect and pile up cold gas in the central regions of the host halo. For the more extended star formation Case 1, the implosion wave collects more material in the center, eventually resulting in a more massive cold core in which star formation can be restarted. The amount of kinetic energy ejected into the IGM is essentially double for Case 2, again because less energy flows towards the center in this run. Blow-away is more efficient if stars form preferentially at the center of the halo.

SN-driven pregalactic outflows may be an efficient mechanism for distributing the product of stellar nucleosynthesis over large cosmological volumes prior to the reionization epoch. In Paper I we used several approximations to show that, for a star formation efficiency of $f_{\star} = 10\%$, the radius of the SN-driven bubble around our prototypical early halo would grow up with time up to a final stalling value of about 11 kpc, when pressure equilibrium with the IGM was achieved. In this simulations we find larger final radii, up to about 26 kpc for both runs. What is the expected spatial extent of the ensemble of wind-driven ejecta from a population of pregalactic systems? In a flat cosmology with $\Omega_M = 1$, $h = 0.5$, $\sigma_8 = 0.63$, $n = 1$, $\Omega_b h^2 = 0.019$, and according to the

Press–Schechter formalism, the comoving abundance of collapsed dark halos with masses $M \approx 10^8 h^{-1} M_\odot$ at $z = 9$ is close to $80 h^3 \text{ Mpc}^{-3}$, corresponding to a mean proper distance between neighboring halos of $15 h^{-1} \text{ kpc}$, a total mass density parameter of order 3 percent, and a stellar density parameter of $0.002 f_*$. Therefore, while with $f_* = 10\%$ only a small fraction, about 4% percent, of the total stellar mass inferred at the present epoch (Fukugita, Hogan, & Peebles 1998) would actually form at these early epochs, the impact of such an era of pregalactic outflows could be quite significant, as the product of stellar nucleosynthesis would be distributed over distance that are comparable to the mean proper distance between neighboring low-mass systems, i.e. volume filling factors of order unity.⁶ The collective explosive output of about ten thousands SNe per $M \gtrsim 10^8 h^{-1} M_\odot$ halo at these early epochs could then pollute the entire intergalactic space to a mean metallicity $\langle Z \rangle = \Omega_Z / \Omega_b \gtrsim 0.003$ (comparable to the levels observed in the Ly α forest at $z \approx 3$) without much perturbing the IGM hydrodynamically, i.e. producing large variations of the baryons relative to the dark matter.

We want to comment here on the possible effect of gas self-gravity, neglected in our simulations. The free-fall time of cold filaments and blobs in the halo ISM is of order $7 \times 10^7 \text{ yr}$ for a gas number density of 1 cm^{-3} , and $2 \times 10^8 \text{ yr}$ for a density ten times greater. This timescale is comparable to the characteristic timescale of gas removal from the potential well of the dark matter halo in our simulations. If the density of the cold component is increased due to self-gravity, radiative cooling will be enhanced. This will decrease the efficiency of the conversion of the available SN energy into the kinetic energy of the outflowing material, weakening the blow-away. Two compensating effects – that act to prevent gas cooling – should also be considered then, photoionization by UV radiation and thermal conduction between the cold and hot interstellar medium.

In particular, the conduction timescale is

$$\tau_{\text{cond}} = \frac{3nkT}{2\nabla \cdot (\kappa T^{5/2} \nabla T)} \approx 4.3 \text{ Myr} \left(\frac{n}{1 \text{ cm}^{-3}} \right) \left(\frac{l}{100 \text{ pc}} \right)^2 \left(\frac{T}{10^7 \text{ K}} \right)^{-5/2}, \quad (27)$$

where κ is the conduction coefficient, n is the gas number density, and l is the characteristic scale length of the cold filaments. Taking $T = 10^7 \text{ K}$, $l = 100 \text{ pc}$, and $n = 1 \text{ cm}^{-3}$ from the results of our simulations, we find $\tau_{\text{cond}} = 4.3 \times 10^6 \text{ yr}$. This timescale is shorter than the free-fall time and comparable to the cooling timescale. The thermal energy of the cold phase will then be affected by thermal conduction from the hot medium.

Finally, while in this paper we simulated the effect of an instantaneous burst of star formation in a protogalactic spherical halo embedded in a uniform IGM, in a series of forthcoming studies we will investigate non-instantaneous stellar feedback in continuous star forming halos of different masses and morphologies, in a cosmological density field. In these cases the blow-away history of the gas may be quite different.

We thank F. Palla, M. Rees, and M. Umemura for useful discussions. This work was started as one of us (A.F.) was a visiting professor at the Center for Computational Physics, Tsukuba University. Support for this project was provided by NASA through ATP grant NAG5-4236 and grant AR-06337.10-94A from the Space Telescope Science Institute, and by a B. Rossi visiting fellowship at the Observatory of Arcetri (P.M.). A.F. and P.M. also acknowledge the support of the EC RTN network “The Physics of the Intergalactic Medium”. The numerical computations were partly carried out on a Hitachi SR8000/8 and a PILOT-3/64 at the Center for Computational Physics, University of Tsukuba, and partly on a Fujitsu VPP-300 at the National Astronomical Observatory in Japan.

REFERENCES

Abel, T., Bryan, G., & Norman, M. 2000, ApJ, 540, 39
 Arora, M. & Roe, P. 1997, J. Comput. Phys., 132, 3
 Barkana, R., & Loeb, A. 2000, PhR, in press (astro-ph/0010468)
 Berger, M. J. & Colella, P. 1989, J. Comput. Phys., 82, 64
 Berger, M. J. & Oliger, J. 1984, J. Comput. Phys., 53, 484
 Bromm, V., Coppi, P. S., & Larson, R. B. 1999, ApJ, 527, L5
 2001a, ApJ, submitted (astro-ph/0102503)
 Bromm, V., Ferrara, A., Coppi, P. S., & Larson, R. B. 2001b, MNRAS, submitted (astro-ph/0104271)
 Bruscoli, M., Ferrara, A., Fabbri, R., & Ciardi, B. 2000, MNRAS, 318, 1068
 Bullock, J. S., Kolatt, T. S., Sigad, Y., Somerville, R. S., Kravtsov, A. V., Klypin, A. A., Primack, J. R., & Dekel, A. 2001, MNRAS, 321, 559
 Burles, S., & Tytler, D. 1998, ApJ, 499, 699
 Cen, R., & Bryan, G. L. 2001, ApJ, 546, L81
 Ciardi, B., Ferrara, A., Governato, F., & Jenkins, A. 2000, MNRAS, 314, 611
 Ciardi, B., Ferrara, A., & Abel, T. 2000, ApJ, 533, 594
 Cole, S. M., et al. 1994, MNRAS, 271, 781
 Colella, P. & Woodward, P. R. 1984, J. Comput. Phys., 54, 174
 D’Ercole, A., & Brightenti, F. 1999, MNRAS, 309, 941
 Dekel, A., & Silk, J. 1986, ApJ, 303, 39
 Efstathiou, G. 2000, MNRAS, 317, 697
 Ellison, S. L., Songaila, A., Schaye, J., & Pettini, M. 2000, AJ, 120, 1167
 Ferrara, A., & Tolstoy, E. 2000, MNRAS, 313, 291
 Ferrara, A., Pettini, M., & Shchekinov, Y. 2000, MNRAS, 319, 539
 Fukugita, M., Hogan, C. J., & Peebles, P. J. E. 1998, ApJ, 503, 518
 Gnedin, N. Y., & Ostriker, J. P. 1997, ApJ, 486, 581
 Heiles, C. 1990, ApJ, 354, 483
 Katz, N. 1992, ApJ, 391, 502
 Lada, C. J., & Wilking, B. A. 1984, ApJ, 287, 610
 Larson, R. B. 1974, MNRAS, 169, 229
 Liou, M.-S., & Steffen, C. J. 1993, J. Comput. Phys., 107, 23
 Machacek, M. E., Bryan, G. L., & Abel, T. 2001, ApJ, 548, 509
 MacLow, M.-M., McCray, R., & Norman, M. L. 1989, ApJ, 337, 141
 MacLow, M.-M., & Ferrara, A. 1999, ApJ, 513, 142
 Madau, P. 2000, Phil. Trans. R. Soc. London A, 358, 2021
 Madau, P., Ferrara, A., & Rees, M. J. 2001, ApJ, 554, *** (Paper I)
 Madau, P., & Rees, M. J. 2001, ApJ, 551, L27
 McKee, C. F., & Williams, J. P. 1997, ApJ, 476, 144
 Mihos, J. C., & Hernquist, L. 1994, ApJ, 437, 611
 Mori, M., Yoshii, Y., & Nomoto, K. 1999, ApJ, 511, 585
 Mori, M., Yoshii, Y., Tsujimoto, T., & Nomoto, K. 1997, ApJ, 478, L21
 Murakami, I., & Babul, A. 1999, MNRAS, 309, 161

⁶We note that, on this assumption, f_* , and hence the early luminosity of these systems, would exceed the value predicted by the usual low-mass extrapolation of CDM galaxy formation models (cf. White & Frenk 1991). In these scenarios f_* is postulated to decline steeply in shallow potential wells, thereby reducing the population of low-luminosity galaxies and avoiding the so-called ‘cooling catastrophe’.

Nath, B., & Trentham, N. 1997, MNRAS, 291, 505
 Navarro, J. F., Frenk, C. S., & White, S. D. M. 1997, ApJ, 490, 493
 Navarro J. F. & White, S. D. M. 1993, MNRAS, 265, 271
 Navarro, J. F., & Steinmetz, M. 1997, ApJ, 478, 13
 Navarro, J. F., & Steinmetz, M. 2000, ApJ, 538, 477
 Nishi, R., & Tashiro, M. 2000, ApJ, 537, 50
 Oey, Y. M. S., & Clarke, C. J. 1997, MNRAS, 289, 570
 Pettini, M., Steidel, C. C., Adelberger, K. L., Dickinson, M., & Giavalisco, M. 2000, ApJ, 528, 96
 Ricotti, M., Gnedin, N., & Shull, J. M. 2000, ApJ, 534, 41
 Ruffert, M. 1992, A&A, 265, 82
 Scannapieco, E., & Broadhurst, T. 2001, ApJ, 549, 28
 Scannapieco, E., Ferrara A., & Broadhurst, T. 2000, ApJ, 536, L11
 Silk, J. 1997, ApJ, 481, 703
 Shull, J. M. & Silk, J. 1979, ApJ, 234, 427
 Songaila, A. 1997, ApJ, 490, L1
 Sutherland, R. S. & Dopita, M. A. 1993, ApJS, 88, 253
 Tegmark, M., Silk, J., & Evrard, A. 1993, ApJ, 417, 54
 Theuns, T., Mo, H. J., & Schaye, J. 2001, MNRAS, 321, 450
 Tomisaka, K. 1996, PASJ, 48, 701
 van Leer, B. 1977, J. Comput. Phys., 32, 104
 Voit, G. M. 1996, ApJ, 465, 548
 Wada, Y., & Liou, M.-S. 1997, SIAM J. Sci. Comput., 18, 633
 Weaver, R., McCay, R., Castor, J., Shapiro, P., & Moore, R., 1977, ApJ, 218, 377
 White, S. D. M., & Frenk, C. S. 1991, ApJ, 379, 52
 Wilking, B. A., & Lada, C. J. 1983, ApJ, 274, 698

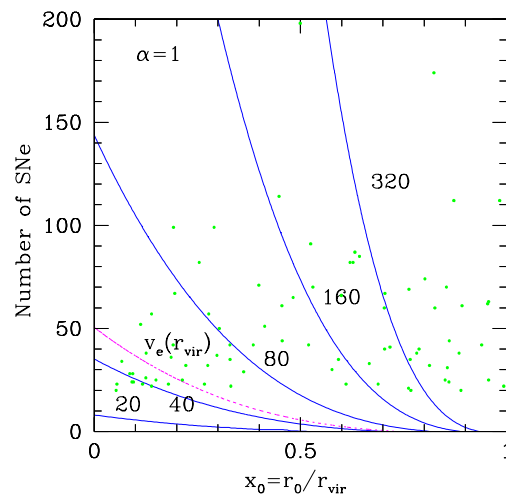


FIG. 1.— Isocontours in the $x_0 - N$ plane of bubble shell velocity, $v_s(r_{vir})$ (in km s^{-1}), at the virial radius. Here N SNe are assumed to explode at a distance x_0 from the center (in units of the halo virial radius). Also shown (dotted line) is the isocontour corresponding to the escape speed $v_e(r_{vir})$. The points indicate the locus of the associations used in the numerical simulations for $\alpha = 1$ (Case 1).

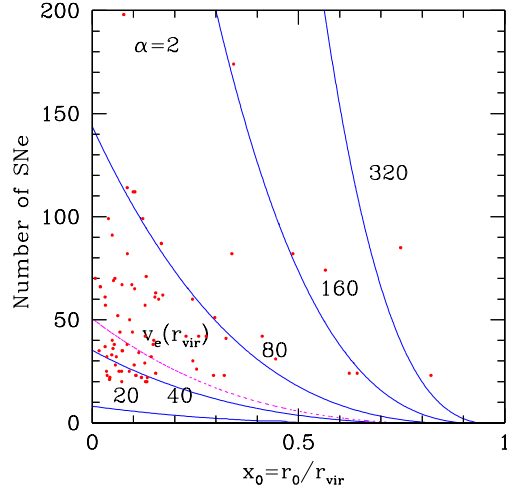


FIG. 2.— Same as Fig. 2, but for $\alpha = 2$ (Case 2).

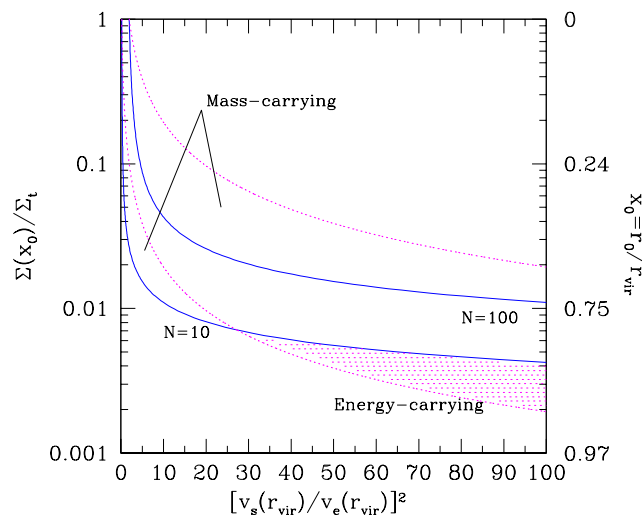


FIG. 3.— Halo gas column density $\Sigma(x_0)$ (normalized to the total gas column density through the halo Σ_t) vs. $[v_s(r_{vir})/v_e(r_{vir})]^2$ for two values of $N = 10, 100$ (solid curves). The dotted lines depict the corresponding curves of constant kinetic energy flux, $\mathcal{E}_k(N)$. The shaded area indicates the parameter space in which the wind is energy-carrying.

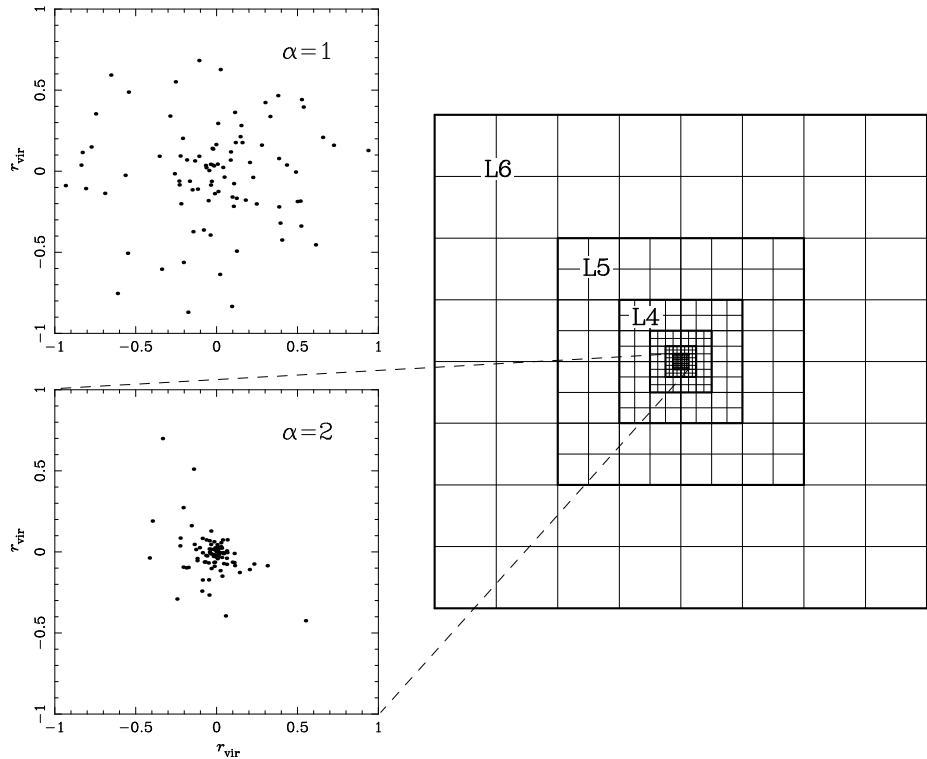


FIG. 4.— *Left:* Projected distributions of OB associations. The upper and lower panels correspond to Case 1 and Case 2, respectively. *Right:* The structure of the nested grids is shown for a two-dimensional sectional plane. Six levels of fixed Cartesian grids were used, with the same number ($128 \times 128 \times 128$) of cells for every level. The box size of the finest grid (L1) was set equal to $2r_{\text{vir}}$, so L1 covers the entire subgalactic halo.

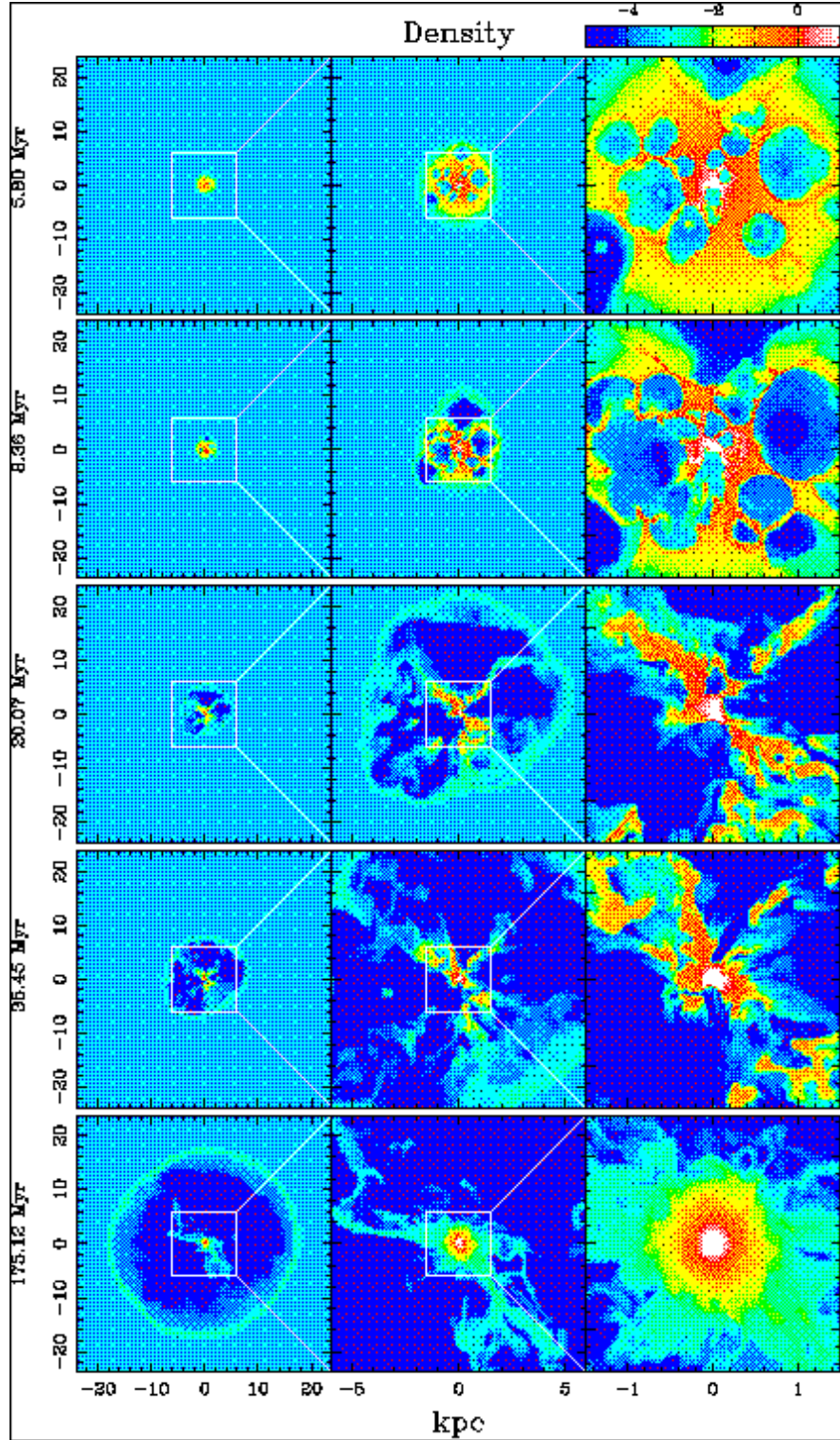


FIG. 5.— Snapshots of the logarithmic number density of the gas at five different elapsed times for our Case 1 simulation run. The three panels in each row show the spatial density distribution in the $X - Y$ plane on the nested grids. The left, middle, and right panels in each row correspond to the level L5, L3, and L1 grid, respectively.

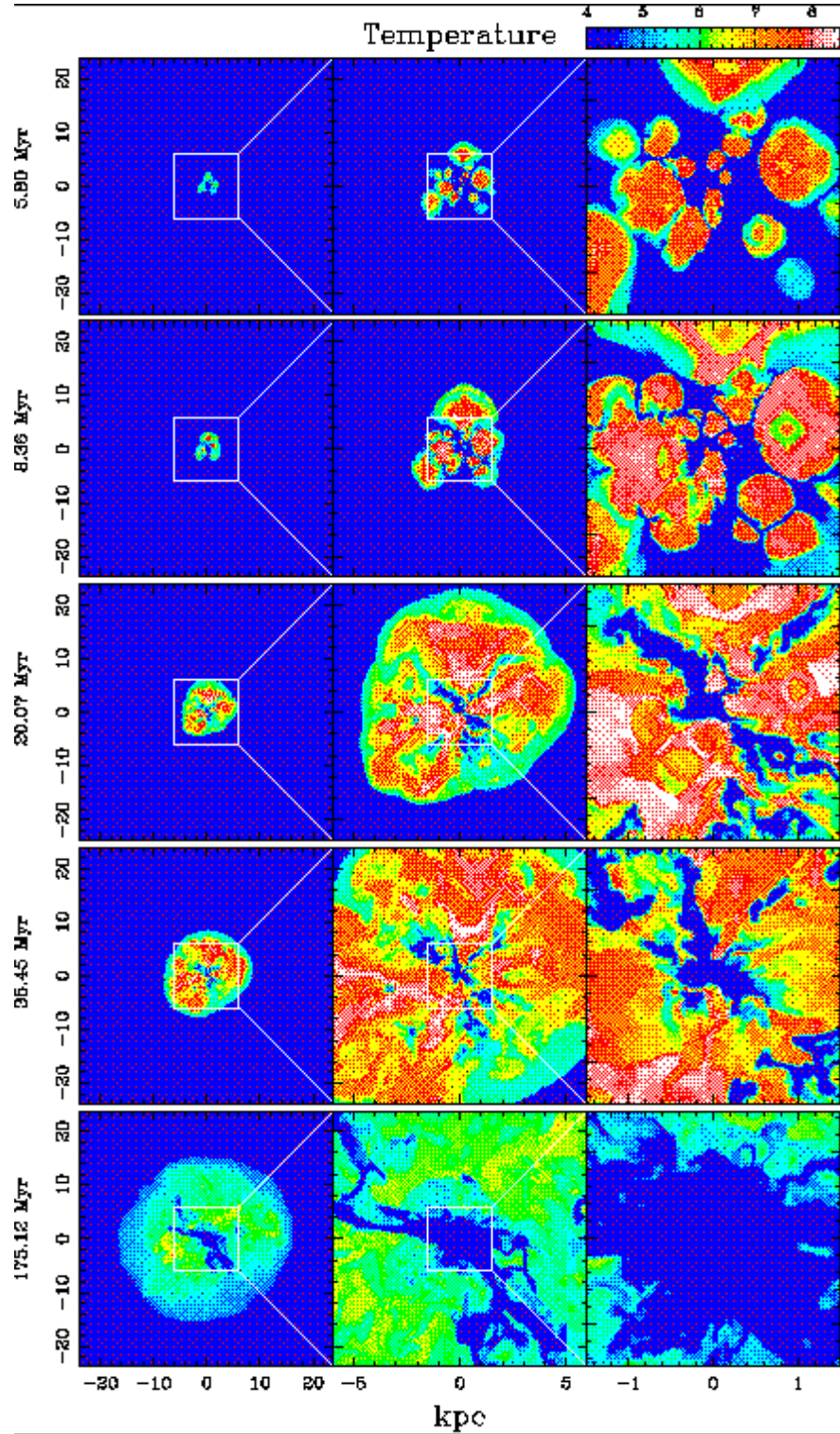


FIG. 6.— Snapshots of the logarithmic temperature of the gas at five different elapsed times for our Case 1 simulation run. The three panels in each row show the spatial temperature distribution in the $X - Y$ plane on the nested grids. The left, middle and right panels in each row correspond to the level L5, L3, and L1 grid, respectively.

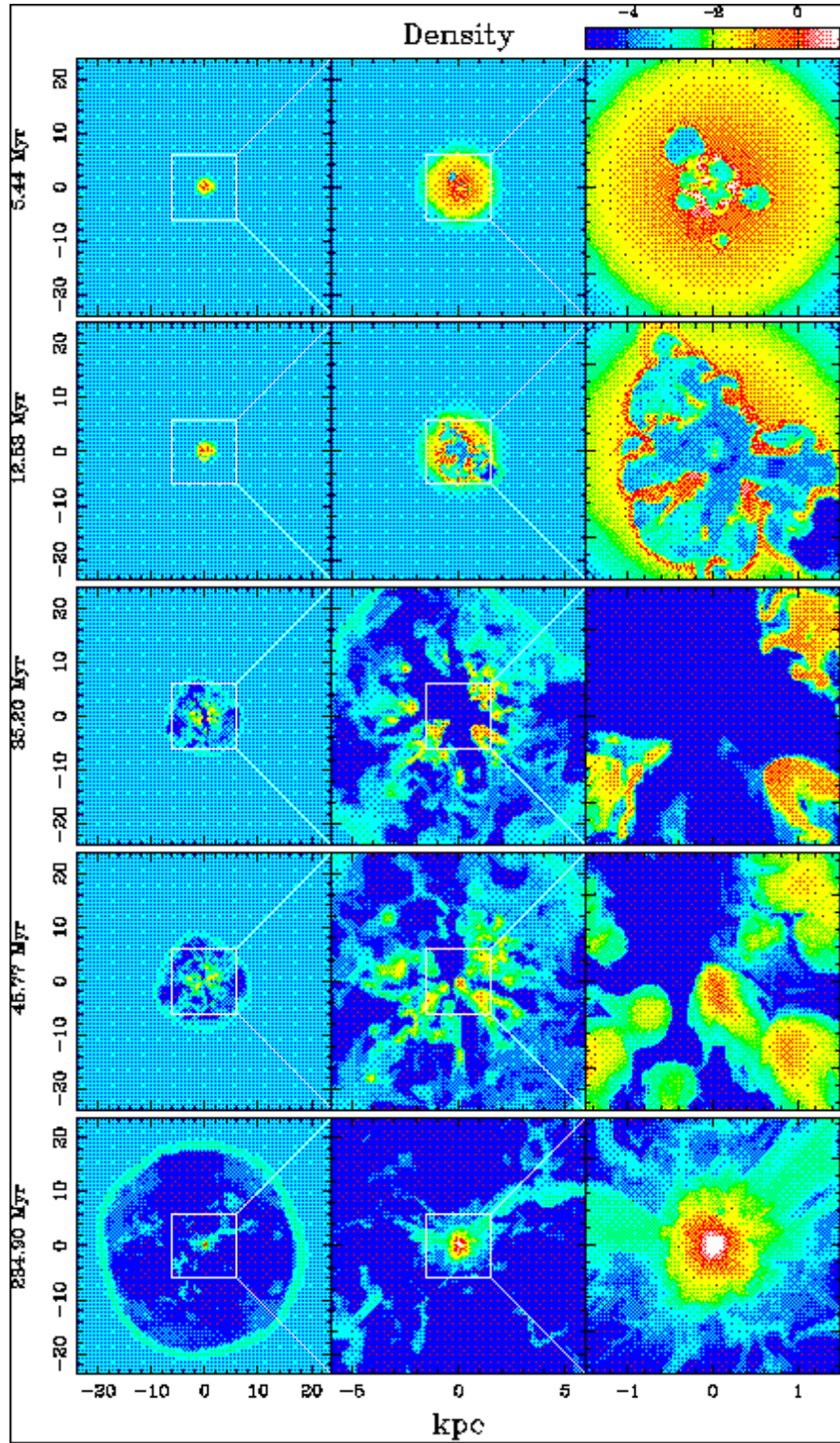


FIG. 7.— Same as in Fig. 7 but for our Case 2 simulation run.

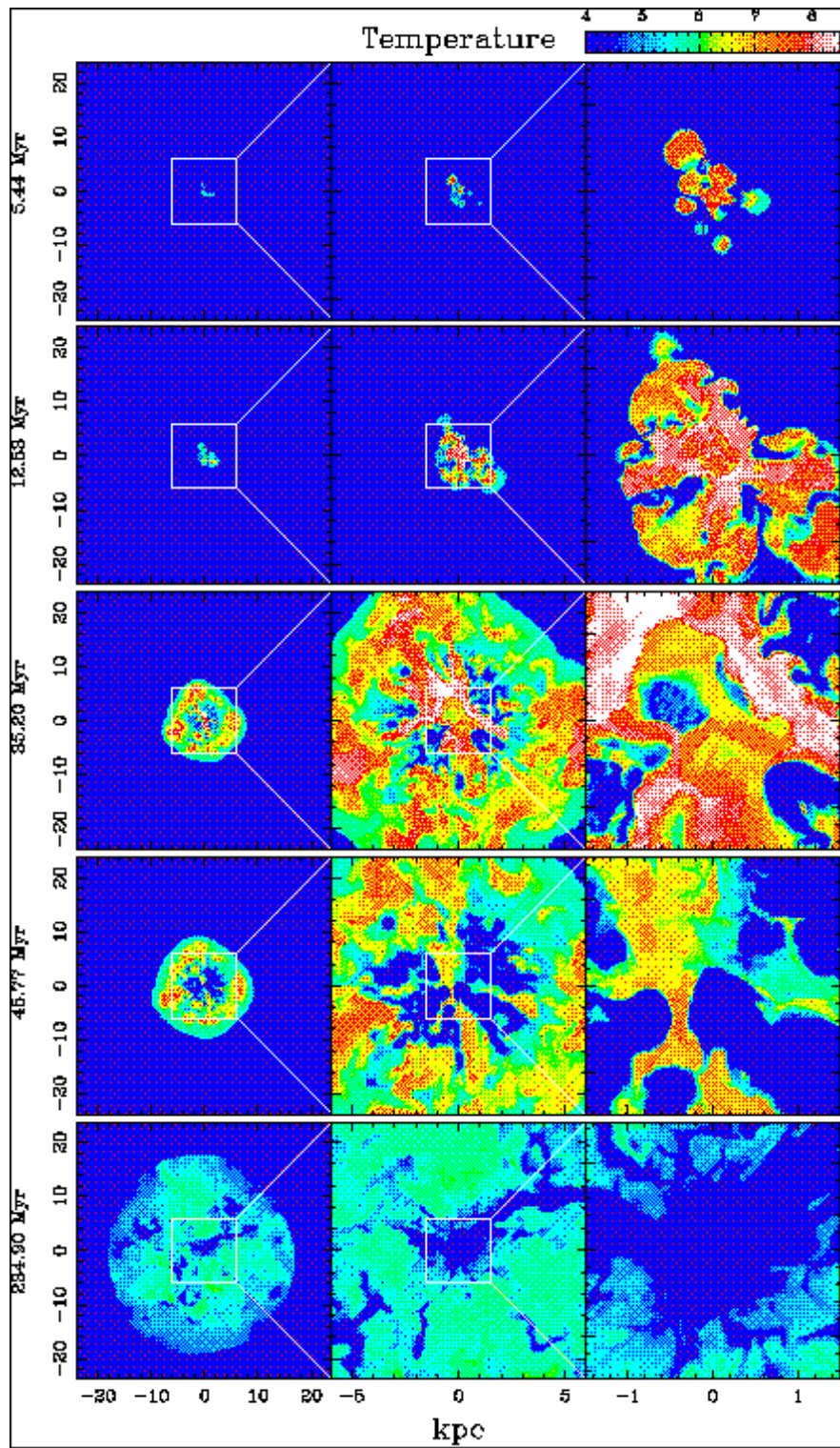


FIG. 8.— Same as in Fig. 8 but for our Case 2 simulation run.

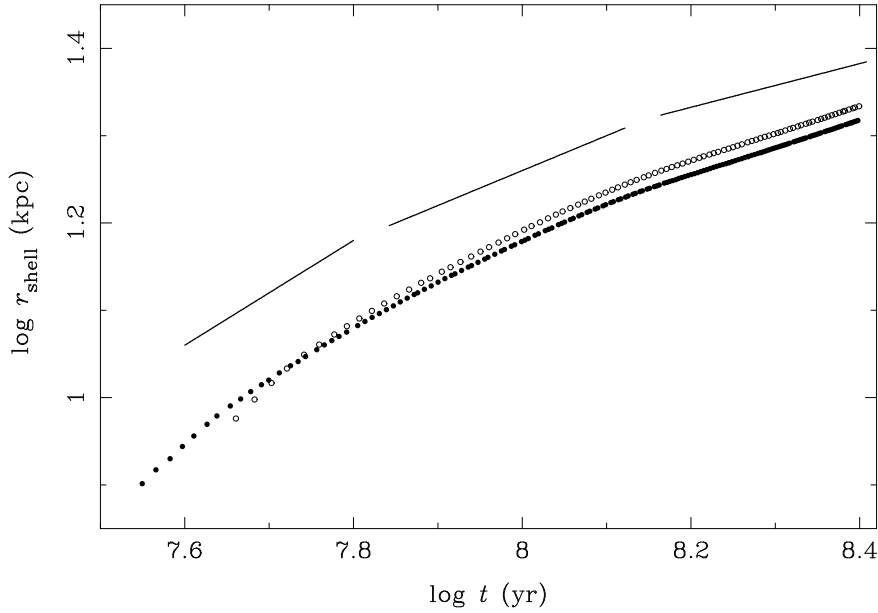


FIG. 9.— The evolution of the shell radius as a function of time. The *filled* (*open*) *circles* correspond to the Case 1 (Case 2) simulation run. The *solid lines* show the expected power–law behavior in the energy–driven phase ($r_{\text{shell}} \propto t^{3/5}$), the adiabatic Sedov–Taylor solution ($r_{\text{shell}} \propto t^{2/5}$), and the momentum–conserving ‘snowplough’ phase ($r_{\text{shell}} \propto t^{1/4}$).

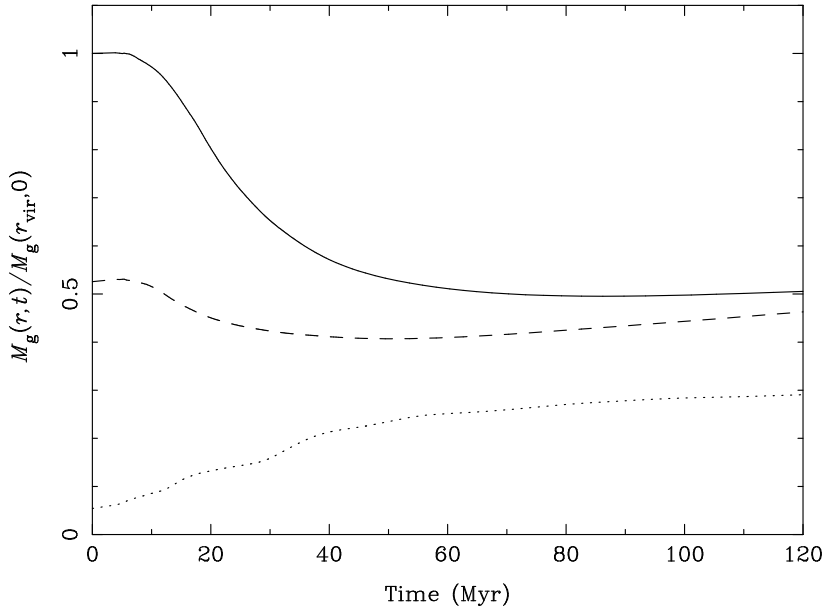


FIG. 10.— The evolution of the gas mass inside the gravitational potential well of the CDM halo for our simulation run of Case 1 ($\alpha = 1$) as a function of time. Curves correspond to the gas mass inside the virial radius r_{vir} (*solid line*), $0.5r_{\text{vir}}$ (*dashed line*), and $0.1r_{\text{vir}}$ (*dotted line*).

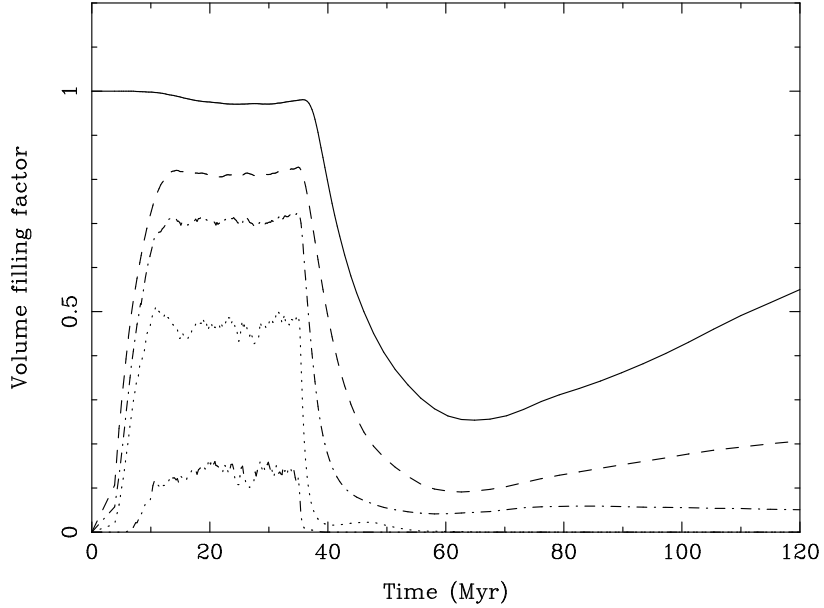


FIG. 11.— Cumulative evolution of the volume filling factor inside the virial radius of the gravitational potential well of the CDM halo for our simulation run of Case 1 ($\alpha = 1$), as a function of time. Each curve corresponds to a different gas temperature (solid line: $T = 10^4$ K, dashed line: $T = 10^5$ K, dash-dotted line: $T = 10^6$ K, dotted line: $T = 10^7$ K, and dash-dot-dotted line: $T = 10^8$ K).

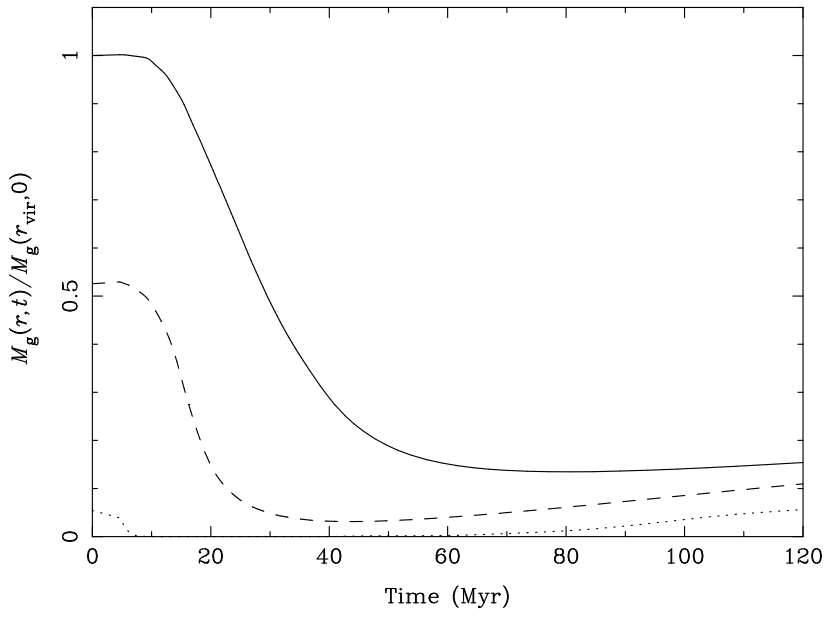


FIG. 12.— Same as in Fig. 12 but for our Case 2 simulation run.

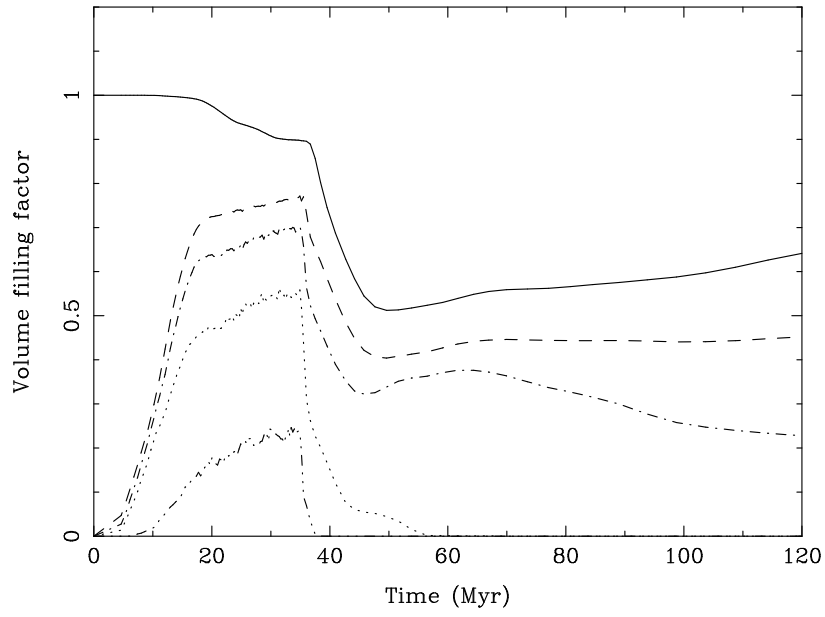


FIG. 13.— Same as in Fig. 13 but for our Case 2 simulation run.

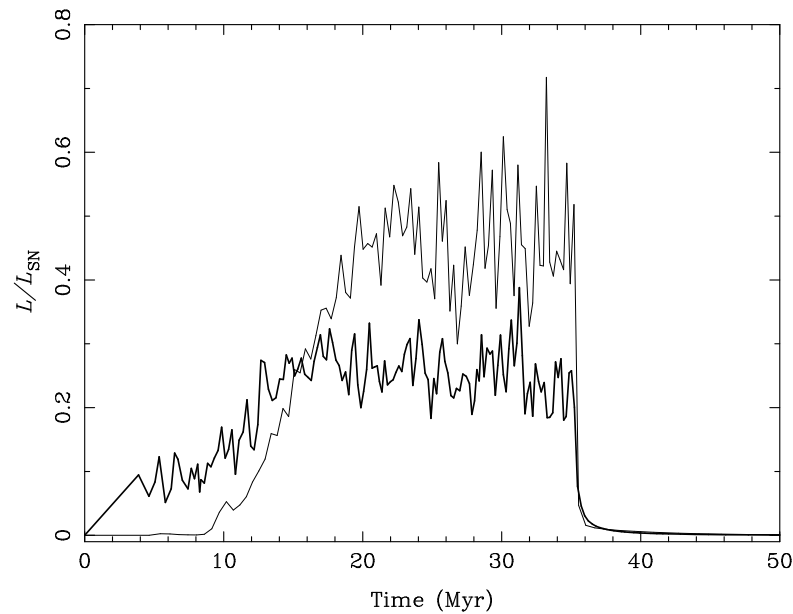


FIG. 14.— Fraction of the SN mechanical luminosity carried by the outflowing gas as kinetic energy through the virial radius, as a function of time. The thick line corresponds to the simulation run of Case 1, and thin line corresponds to that of Case 2.